Check for updates

ATMOSPHERIC SCIENCE

Intensification of East Asian summer extreme precipitation under a net-zero anthropogenic CO_2 emission scenario

Seungmok Paik[1], Daehyun Kim[1]*, Soon-Il An[2]*, So-Eun Park[2], Andrew D. King[3,4], Seung-Ki Min[5], Chao Liu[1], Jongsoo Shin[6]

Copyright © 2026 The Authors, some rights reserved; exclusive licensee American Association for the Advancement of Science. No claim to original U.S. Government Works. Distributed under a Creative Commons Attribution NonCommercial License 4.0 (CC BY-NC).

Global warming has intensified extreme precipitation, a trend projected to continue as warming persists. However, how extreme precipitation characteristics respond to global warming mitigation strategies remains poorly understood. This study examines East Asian summer extreme precipitation responses under a net-zero anthropogenic carbon dioxide (CO_2) emission scenario. Despite substantial cooling over East Asia following atmospheric CO_2 concentration decline, the intensity of extreme precipitation events continues to increase for about 30 years and does not subsequently weaken. This counterintuitive result arises mainly from intensified upward motion during extreme precipitation events, driven by enhanced baroclinicity and strengthening of the upper-tropospheric jet, which together overcompensate the cooling effect. These are essentially due to the hysteresis in the Atlantic (i.e., Atlantic Meridional Overturning Circulation slowdown), Southern (i.e., sustained warming), and Pacific (i.e., El Niño–like warming) Oceans. Our findings highlight that achieving net-zero anthropogenic CO_2 emissions is insufficient to mitigate intensifying extreme rainfall events in the densely populated East Asian countries.

INTRODUCTION

Extreme precipitation is one of the most impactful hydroclimatic events, often triggering floods that threaten lives and livelihoods. Under global warming, extreme precipitation is expected to intensify, primarily due to the increased capacity of the atmosphere to hold moisture at a rate of ~7% per degree of warming, following the Clausius-Clapeyron relationship (*1*). Historically, such warming-driven intensification of extreme precipitation has been observed and attributed to anthropogenic radiative forcings, mostly due to increasing greenhouse gas emissions (*2*–*4*). Future projections based on climate model simulations suggest that this intensifying trend is likely to continue across most regions of the world as global warming persists (*5*–*7*), while regional extreme precipitation responses can be modulated by changes in vertical motion (*5*–*9*).

To achieve the goals of the Paris Agreement (*10*), it is likely necessary to reduce anthropogenic carbon dioxide (CO_2) emissions as much as possible toward net-zero or even net-negative global CO_2 emissions. Consequently, there is growing interest in understanding how climate and weather systems adjust after net-zero CO_2 emissions, which may substantially differ from scenarios of continued CO_2 emissions (*11*–*22*).

East Asia is projected to experience intensified extreme precipitation in summer under continued global warming (*23*, *24*). In CO_2 removal simulations, the frequency of summer daily precipitation exceeding 30 mm day^{-1} over East Asia is projected to decrease during the CO_2 ramp-down period but with a rate that is lower than the rate of increase during the CO_2 ramp-up period (*25*). This hysteresis has been attributed to enhanced moisture convergence associated with northwestward propagating wave responses to an El Niño–like equatorial Pacific warming pattern (*25*). More recently, intensified extreme precipitation during the CO_2 ramp-down phase relative to the CO_2 ramp-up phase has also been reported in CO_2 removal simulations and was attributed to increased seasonal-mean moisture fluxes (i.e., thermodynamic contributions), driven by changes in sea surface temperature warming patterns (*26*). However, changes in East Asian summer extreme precipitation intensity and their underlying physical mechanisms after the achievement of net-zero CO_2 emissions remain poorly understood. In particular, more detailed diagnostics of extreme precipitation events, which are shaped by changes in the large-scale environment, are needed to explicitly elucidate the underlying processes. To address this gap and enhance our understanding, we investigate how East Asian summer extreme precipitation responds under a net-zero anthropogenic CO_2 emission scenario, with particular focus on changes in extreme precipitation intensity. We examine the contributions from thermodynamic and dynamic factors, along with changes in the associated atmospheric conditions during extreme precipitation events. We also examine the role of changes in planetary-scale climatological environments that drive these responses. Our analysis is based on a four-member ensemble of simulations conducted under a net-zero anthropogenic CO_2 emission scenario using Community Earth System Model Version 2 [CESM2 (*27*)] (Materials and Methods).

RESULTS

Characteristics of East Asian summer extreme precipitation

We first identify extreme precipitation events [>99th percentile of 6-hourly precipitation during June to August (JJA); Materials and Methods] and characterize their concurrent atmospheric conditions by averaging instantaneous atmospheric fields at the start and end of each 6-hour period (e.g., 00 to 06 UTC precipitation, with instantaneous atmospheric conditions averaged over 00 UTC and 06 UTC) by using the CESM2 present-day simulation (Materials and Methods) (Fig. 1). Composite synoptic circulation patterns for

[1]School of Earth and Environmental Sciences, Seoul National University, Seoul, South Korea. [2]Department of Atmospheric Sciences, Yonsei University, Seoul, South Korea. [3]School of Geography, Earth, and Atmospheric Sciences, University of Melbourne, Melbourne, Victoria, Australia. [4]Australian Research Council Centre of Excellence for 21st Century Weather, Melbourne, Victoria, Australia. [5]Division of Environmental Science and Engineering, Pohang University of Science and Technology, Pohang, South Korea. [6]Physical Oceanography Department, Woods Hole Oceanographic Institution, Woods Hole, MA, USA.
*Corresponding author. Email: daehyun@snu.ac.kr (D.K.); sian@yonsei.ac.kr (S.-I.A.)

Downloaded from https://www.science.org on November 08, 2026

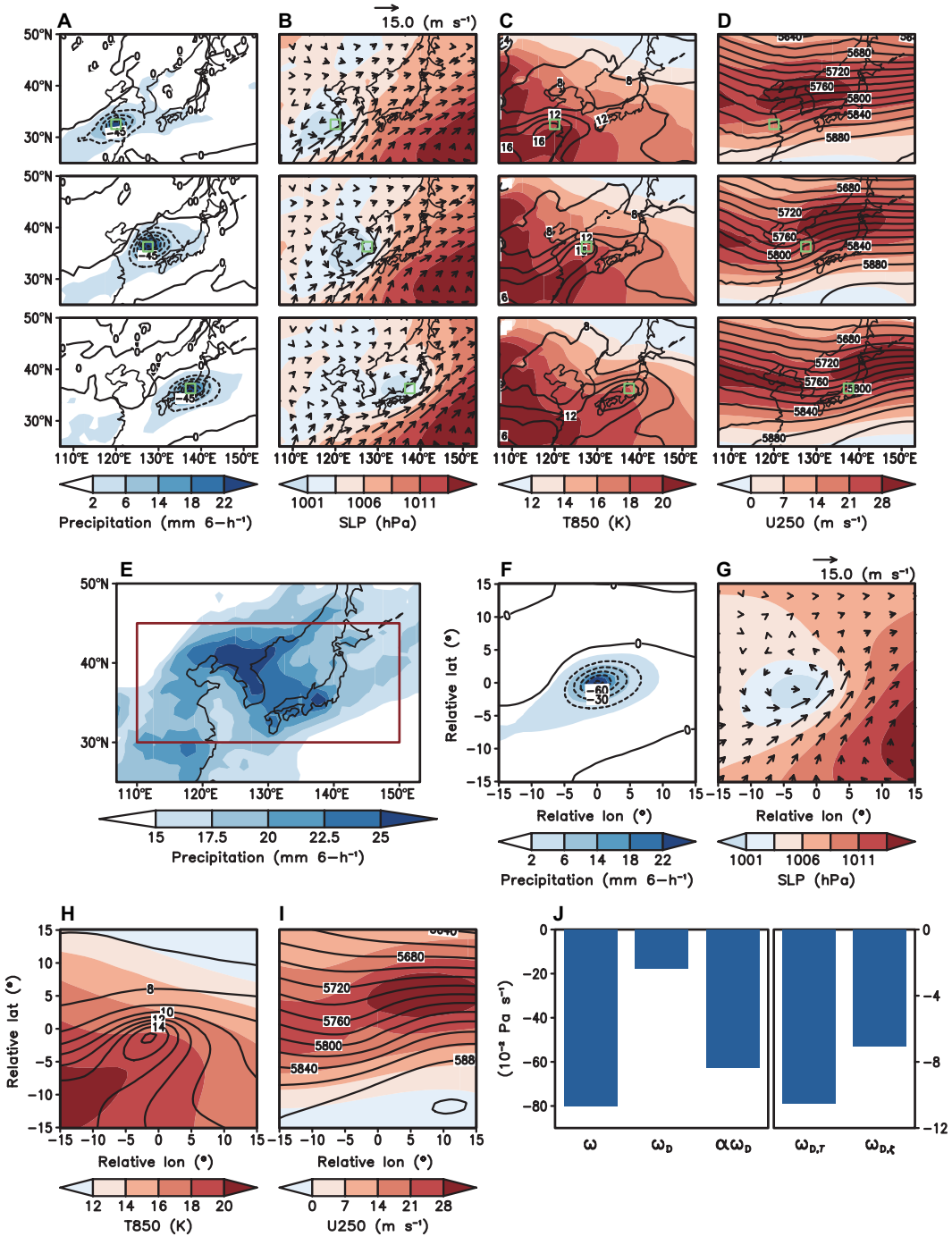


Fig. 1. Characteristics of East Asian summer extreme precipitation. (**A** to **D**) Composite synoptic patterns associated with extreme precipitation events (>99th percentile of 6-hourly precipitation during JJA) at selected grid points (green boxes) in (top row) China, (middle row) South Korea, and (bottom row) Japan in the CESM2 present-day simulation for (A) precipitation (shading; mm 6-h^{-1} denotes mm per 6 hours) and 500-hPa vertical motion (contours; interval: 15 × 10^{-2} Pa s^{-1}), (B) sea level pressure (SLP; shading) and 850-hPa horizontal winds (vectors), (C) 850-hPa temperature (T850; shading) and specific humidity (contours; interval: 2 g kg^{-1}), and (D) 250-hPa zonal wind (U250; shading) and 500-hPa geopotential height (contours; interval: 20 m). h, hour. (**E**) Spatial pattern of the threshold for extreme precipitation (99th percentile of 6-hourly precipitation during JJA) at each grid point in the CESM2 present-day simulation. The red box outlines the East Asia domain. (**F** to **J**) Centered composite of (F) precipitation (shading) and 500-hPa vertical motion (contours; interval: 15 × 10^{-2} Pa s^{-1}), (G) SLP (shading) and 850-hPa horizontal winds (vectors), (H) 850-hPa temperature (T850; shading) and specific humidity (contours; interval: 1 g kg^{-1}), (I) 250-hPa zonal wind (U250; shading) and 500-hPa geopotential height (contours; interval: 20 m), and (J) 500 hPa vertical motion (ω), adiabatic quasi-geostrophic vertical motion (ω_D), feedback based on ω_D ($\alpha\omega_D$), the temperature advection term in ω_D ($\omega_{D,T}$), and the vorticity-advection term in ω_D ($\omega_{D,\zeta}$) [(F) to (I) show a ±15° latitude-longitude square centered on the extreme precipitation events, and (J) shows the values at grid points where extreme precipitation events occur] associated with extreme precipitation events over East Asia {grids are aggregated across 110°E to 150°E, 30°N to 45°N; restricted to regions where the extreme precipitation threshold exceeds 15 mm 6-hour^{-1} [displayed in (E)]} during JJA in the CESM2 present-day simulation.

Downloaded from https://www.science.org on November 08, 2026

extreme precipitation events at selected grid points within China, South Korea, and Japan [green boxes in Fig. 1 (A to D)] exhibit common features (99th percentile threshold shown in Fig. 1E), including pronounced (i) upward motion at 500 hPa (Fig. 1A), (ii) low-level cyclonic circulation (Fig. 1B), (iii) lower-tropospheric horizontal gradients of temperature and specific humidity (i.e., strong baroclinicity) (Fig. 1C), and (iv) an upper-level trough located west of the events and along the southern flank of the upper-level jet entrance (Fig. 1D). The threshold magnitude of extreme precipitation over East Asia in JJA exceeds 15 mm 6-hour^{-1} across most regions, reaching 25 mm 6-hour^{-1} in some areas (e.g., Korean Peninsula) (Fig. 1E). On average, over East Asia during JJA, extreme precipitation events are accompanied by presented atmospheric conditions: strong upward motion at 500 hPa (Fig. 1F) and low-level cyclonic circulation (Fig. 1G) in which southwesterly winds transport warm, moist air, resulting in a pronounced horizontal gradient of air temperature and abundant moisture (i.e., strong baroclinicity) near where heavy rainfall events occur (Fig. 1H). Such lower-tropospheric atmospheric states are associated with low-pressure systems, atmospheric rivers, and meteorological fronts (*28*–*30*). Extreme precipitation events in East Asia also typically occur near the entrance region of the upper-tropospheric jet (i.e., the eastern side of a trough), with the jet's maximum westerly wind located to the northeast of the events (Fig. 1I), as the southern flank of the jet entrance is usually characterized by upper-level divergence and low-level convergence.

Very strong upward motion (Fig. 1F) is essentially what makes the extreme precipitation events extreme. According to the view in which the vertical motion originates as the ageostrophic component in the quasi-geostrophic system and is then amplified by feedbacks from diabatic processes [e.g., Nie *et al.* (*9*)], the vertical motion at 500 hPa (ω) can be expressed as $\omega = \omega_D + \alpha\omega_D = \omega_D(1+\alpha)$, where ω_D represents the adiabatic quasi-geostrophic ω, and α represents the amplification factor associated with diabatic heating feedback (Materials and Methods). Figure 1J shows that, on average, the total ω is about 4.6 times greater than ω_D (i.e., $\alpha \cong 3.6$). Further decomposition of ω_D into the temperature-advection term ($\omega_{D,T}$) and vorticity-advection term ($\omega_{D,\zeta}$) ($\omega_D = \omega_{D,T} + \omega_{D,\zeta}$; Materials and Methods) indicates that both terms contribute substantially (Fig. 1J). Large contributions from $\omega_{D,T}$indicate the crucial role of baroclinicity, while $\omega_{D,\zeta}$ highlights the importance of the upper-level trough to the west, with both reflecting the common importance of the westerly jet associated with extreme precipitation events (Fig. 1, H to J). These findings are consistent with evidence from IMERG observations (*31*) and ERA5 reanalysis (fig. S1) (*32*).

East Asian summer extreme precipitation responses under a net-zero anthropogenic CO_2 emission scenario

In the CESM2 simulations analyzed, anthropogenic CO_2 emissions increase until 2050 and then decline to zero in 2123, remaining at that level thereafter (Fig. 2A; Materials and Methods). Atmospheric CO_2 concentrations peak during the emission decline phase, reaching 724.3 parts per million (ppm) in 2106, and subsequently decrease to 607.4 ppm by 2300 (Fig. 2A). Over East Asia, near-surface air temperature during JJA exhibits a quasi-monotonic response to changes in atmospheric CO_2 concentrations (Fig. 2B). Although the warming signal appears to peak earlier than the CO_2 concentration (Fig. 2B), it is an artifact of the 31-year moving average, reflecting rapid cooling following peak CO_2 concentration, likely further amplified by the continued weakening of the Atlantic Meridional Overturning Circulation (AMOC) (fig. S2) (*13*, *17*, *33*, *34*). However, despite the cooling following peak CO_2, the mean intensity of extreme precipitation events in each 31-year window continues to increase substantially for about 30 years, with a few additional increases during the 23rd century rather than any subsequent weakening, remaining about 23 to 24% stronger than in the present day through 2300 (Fig. 2B). The individual ensemble simulations show responses that are broadly consistent with the main findings based on the ensemble mean (fig. S3). Figure 2 (C and D) shows the spatial patterns of extreme precipitation intensity anomalies relative to the present day for two periods: (i) 2091 to 2121 (a 31-year window centered on peak CO_2, corresponding to the maximum in the 31-year moving average; hereafter the "peak CO_2" period) and (ii) 2170 to 2200 (the final 31 years of the 22nd century; hereafter the "net-zero" period). Compared to those during the peak CO_2 period, the extreme precipitation intensity changes during the net-zero period are overall stronger, especially in the coastal areas of China, Korea, and Japan.

Contribution analysis of changes in East Asian summer extreme precipitation

As extreme precipitation intensifies despite CO_2 emission reductions and cooling over East Asia (Fig. 2, B to D), its sensitivity to near-surface temperature changes during the net-zero period is greater than that of the peak CO_2 period (Fig. 3A), indicating that factors other than the local warming play a critical role. We conducted a contribution analysis (Materials and Methods) by decomposing changes in extreme precipitation intensity per degree of local warming into thermodynamic, dynamic, and nonlinear components. The sum of the three components closely matches the simulated changes in extreme precipitation intensity (Fig. 3, A and B). Figure 3C shows that thermodynamic contributions [effects of Δ(near-surface specific humidity); Δ indicates anomalies relative to present-day averages] are comparable between the peak CO_2 and net-zero periods. Most of the difference between the two periods can be attributed to the dynamic contributions (effects of $\Delta\omega$), which are markedly greater during the net-zero period compared to the peak CO_2 period (Fig. 3D). Nonlinear components have negligible influence (fig. S4). Area-averaged values in Fig. 3E clearly show that the greater extreme precipitation intensification per unit warming during the net-zero period is primarily driven by dynamic factors, reflecting a systematic difference in ω between the two periods.

Physical mechanisms underlying enhanced upward motion

As shown earlier, summertime extreme precipitation events in East Asia are accompanied by distinct atmospheric conditions, including pronounced lower-tropospheric baroclinicity and a westerly jet (Fig. 1, G to I). Figure 4 shows differences in those atmospheric conditions during extreme precipitation events between the peak CO_2 and the net-zero periods. Relative to the peak CO_2 period, the net-zero period exhibits stronger air temperature and density gradients in the meridional direction (Fig. 4A), which would enhance temperature advection in the lower troposphere. The enhanced baroclinicity is associated with the stronger jet throughout the troposphere (Fig. 4B). Horizontal patterns also show an enhanced upper-tropospheric jet (Fig. 4C), expected to strengthen vorticity advection with a comparable magnitude upper-level trough to the west of the extreme precipitation events (Fig. 4D; patterns for individual peak CO_2 and net-zero periods are presented in fig. S5). Composite synoptic circulation patterns for

Downloaded from https://www.science.org on November 08, 2026

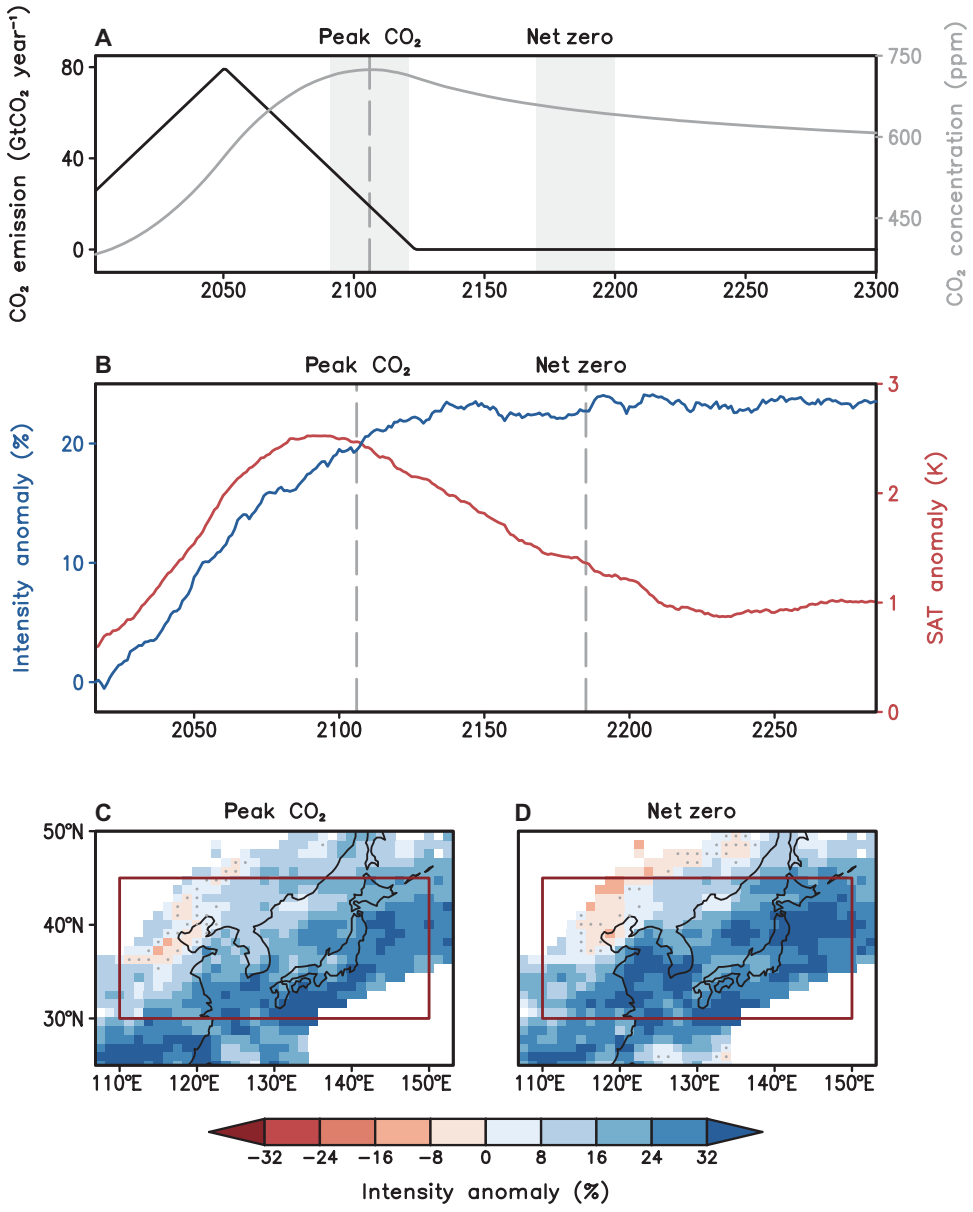


Fig. 2. East Asian summer extreme precipitation intensity responses under a net-zero anthropogenic CO_2 emission scenario. (**A**) Time series of prescribed anthropogenic CO_2 emissions (black) and simulated global annual mean atmospheric CO_2 concentrations (gray) from 2001 to 2300, with concentrations averaged over four CESM2 ensemble simulations. Light gray shading denotes two analysis periods: (i) 2091 to 2121 ("peak CO_2" period), a 31-year window centered on the peak CO_2 concentration in 2106 (vertical dashed gray line), and (ii) 2170 to 2200 ("net-zero" period), the final 31 years of the 22nd century. (**B**) Time series of 31-year moving averages of near-surface air temperature (SAT) anomalies (red) and percent anomalies in extreme precipitation intensity (blue; average of 6-hourly precipitation events exceeding the 99th percentile within each 31-year window) during JJA, relative to present-day means, averaged over East Asia [110°E to 150°E, 30°N to 45°N; only grids where the present-day extreme precipitation threshold exceeds 15 mm 6-hour^{-1} (displayed in Fig. 1E) are considered]. Vertical dashed gray lines denote the peak CO_2 and net-zero periods. (**C** and **D**) Spatial patterns of percent anomalies in extreme precipitation intensity (average of 6-hourly precipitation >99th percentile) during JJA for the (C) peak CO_2 period and (D) net-zero period, relative to present-day means. Results are shown only for regions where the present-day extreme precipitation threshold exceeds 15 mm 6-hour^{-1} (displayed in Fig. 1E). Gray dots indicate regional changes that are not statistically significant at the 5% level (Materials and Methods). The red box outlines the East Asia domain.

extreme precipitation events at selected grid points within China, South Korea, and Japan show that differences between the two periods consistently feature stronger extreme precipitation accompanied by an enhanced upward motion, which appears to be driven by intensified horizontal baroclinicity and upper-level jet stream (fig. S6).

The enhanced baroclinicity (Fig. 4A) and the associated acceleration of the tropospheric jet (Fig. 4B) are expected to strengthen $\omega_{D,T}$ primarily through increased temperature advection, and the acceleration of the upper-tropospheric jet (Fig. 4, B and C) is expected to strengthen $\omega_{D,\zeta}$ through stronger vorticity advection. Changes in the individual components of ω_D, the temperature-advection term ($\omega_{D,T}$),

Downloaded from https://www.science.org on November 08, 2026

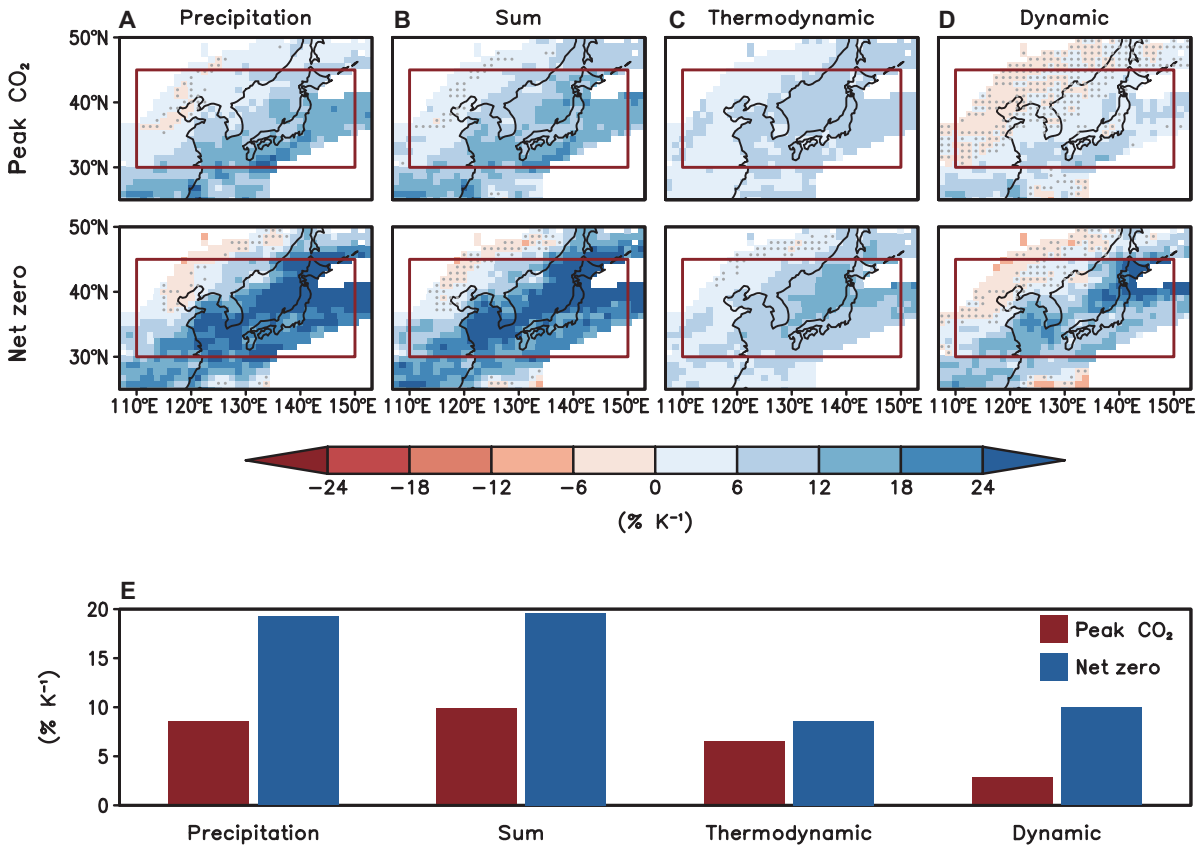


Fig. 3. Contribution analysis of changes in East Asian summer extreme precipitation intensity. (**A**) Spatial patterns of percent anomalies in extreme precipitation intensity (average of 6-hourly precipitation >99th percentile) per unit of local near-surface warming during JJA for the (upper row) peak CO_2 period and (lower row) net-zero period, relative to present-day averages. Results are shown only for regions where the present-day extreme precipitation threshold exceeds 15 mm 6-hour^{-1} (displayed in Fig. 1E) and the near-surface warming anomaly during the net-zero period is at least 0.5 K. Gray dots indicate regional changes that are not statistically significant at the 5% level (Materials and Methods). The red box outlines the East Asia domain. (**B** to **D**) Same as (A) but for (B) the combined effects of thermodynamic, dynamic, and nonlinear components; (C) contributions from thermodynamic factors; and (D) contributions from dynamic factors. Percent values are calculated by dividing the present-day $\omega \times q$ (ω: 500-hPa vertical motion; q: near-surface specific humidity) averages and then scaled per degree of near-surface warming. Significance is tested for whether changes in the individual terms contribute significantly to the change in $\omega \times q$. (**E**) East Asia–averaged [110°E to 150°E, 30°N to 45°N; mean of nonmissing grid values within the red box in (A) to (D)] changes in (from left to right) extreme precipitation; the combined effects of thermodynamic, dynamic, and nonlinear components; contributions from thermodynamic factors; and dynamic factors during JJA for the (red) peak CO_2 period and (blue) net-zero period.

and vorticity-advection term ($\omega_{D,\zeta}$) (Fig. 5A) show that both significantly contribute to the intensification of ω_D. The percentage increase is larger for $\omega_{D,T}$ than for $\omega_{D,\zeta}$ (Fig. 5A), while $\omega_{D,T}$ also has a larger climatological magnitude (Fig. 1J), highlighting the particularly important role of the enhanced baroclinicity. As a result, ω_D strengthens by 10.2% from the peak CO_2 period to the net-zero period (Fig. 5B). In contrast, $(1+\alpha)$ decreases by 4.8% (Fig. 5B), partly compensating the effect of enhanced ω_D. The reduction in α is likely associated with the lower column water vapor (fig. S7). Consequently, ω strengthens significantly by 5.3%, indicating enhanced upward motion (Fig. 5B) and thereby intensifying extreme precipitation.

Last, we examine changes in planetary-scale environmental conditions that affect the atmospheric state associated with extreme precipitation events in East Asia. During the peak CO_2 period, warming is stronger in the Northern Hemisphere (NH) extratropics than in the tropics (upper panel of Fig. 6A), weakening the meridional temperature gradient. Concurrently, El Niño–like warming develops in the tropical Pacific [upper panel of Fig. 6A; also during boreal winter (fig. S8A)], which excites a stationary Rossby wave train that induces a high-pressure anomaly over the subtropical western North Pacific and a low-pressure anomaly over the mid-latitude North Pacific (upper panel of Fig. 6B) (CESM2's ability to capture the responses is shown in fig. S9) (*25*, *35*). In the net-zero period, surface temperature largely recovers in the NH extratropics, while the Southern Hemisphere (SH) continues to warm (lower panel of Fig. 6A; see Fig. 6E for their difference). The El Niño–like warming also intensifies (also during boreal winter, as shown in fig. S8), accompanied by modest additional warming or marginal cooling in the equatorial ocean. These surface temperature anomaly patterns are aligned with previous suggestions under CO_2 reduction scenarios (*13*, *16*, *17*, *34*, *36*). Oh *et al.* (*36*) highlighted the role of slow oceanic heat release, particularly in weakly stratified regions such as the Southern Ocean and the eastern tropical Pacific. In addition, the lagged and persistent weakening of the AMOC (fig. S2B) may further reinforce this warming pattern and contribute to the rapid cooling in the NH extratropics (*13*, *17*, *33*, *34*). The stronger SH warming relative to the NH drives a southward shift of the Intertropical Convergence Zone (ITCZ) (*34*) during the net-zero period (fig. S10). The intensified El Niño–like

Downloaded from https://www.science.org on November 08, 2026

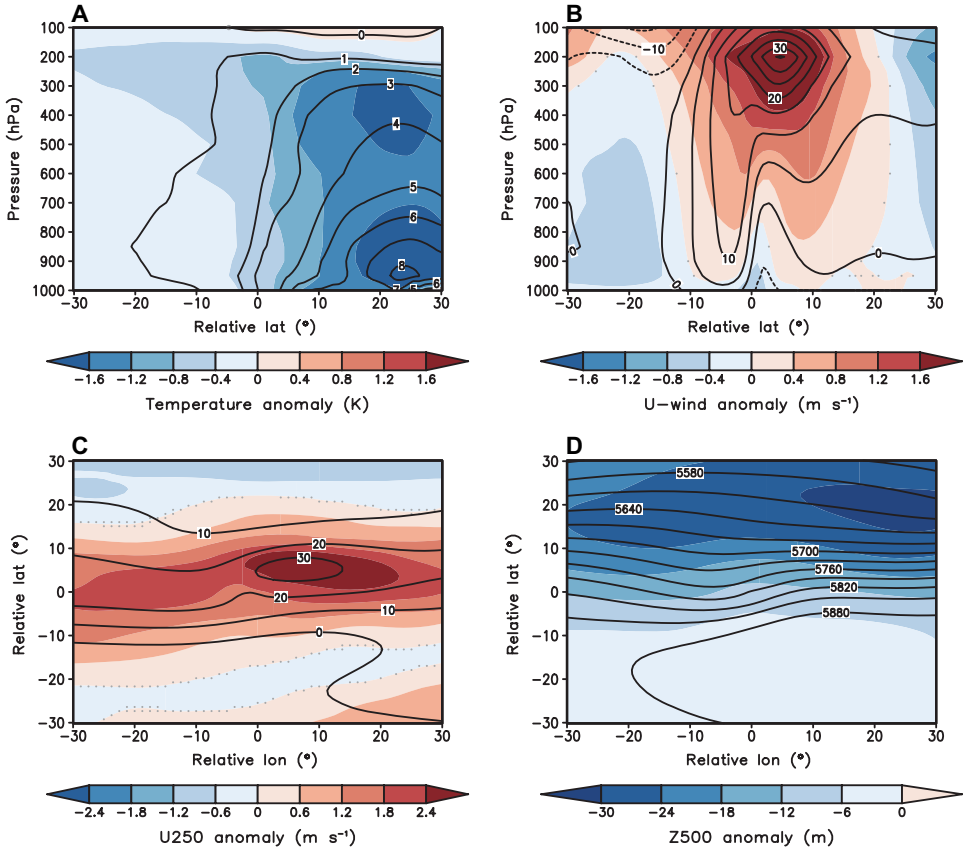


Fig. 4. Changes in atmospheric conditions associated with extreme precipitation events. (**A** and **B**) Zonal-mean composites (−2.5° to 2.5° longitude averages centered on extreme precipitation events) of (A) air temperature (shading) and air density (contours; unit: 10^{-3} kg m^{-3}), (B) zonal wind (U-wind) associated with extreme precipitation events over East Asia [110°E to 150°E, 30°N to 45°N; restricted to regions where the present-day extreme precipitation threshold exceeds 15 mm 6-hour^{-1} (displayed in Fig. 1E)] during JJA, shown as anomalies during the net-zero period relative to the peak CO_2 period. Gray dots indicate regional changes that are not statistically significant at the 5% level (Materials and Methods). Black contours show present-day averages. (**C** and **D**) Same as (A) and (B) but without the zonal mean and shown over a ±30° latitude-longitude square centered on the extreme precipitation events for (C) 250-hPa zonal wind (U250) and (D) 500-hPa geopotential height (Z500). Gray dots indicate regional changes that are not statistically significant at the 5% level (Materials and Methods). Black contours show present-day averages.

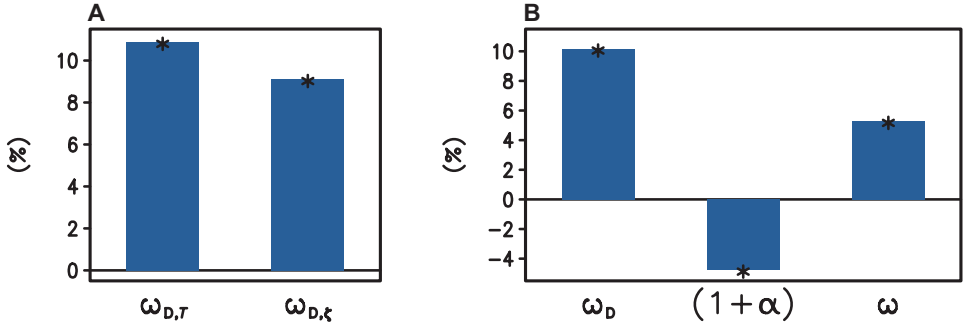


Fig. 5. Changes in decomposed components of vertical motion. Composited anomalies of East Asian extreme precipitation events (110°E to 150°E, 30°N to 45°N; restricted to regions where the present-day extreme precipitation threshold exceeds 15 mm 6-hour^{-1} [displayed in Fig. 1E)] during JJA for the net-zero period relative to the peak CO_2 period for (**A**) components of adiabatic quasi-geostrophic vertical motion (ω_D), including temperature-advection term ($\omega_{D,T}$) and vorticity-advection term ($\omega_{D,\zeta}$), and (**B**) ω_D, $(1+\alpha)$ (the multiplicative feedback factor for ω_D), and 500-hPa vertical motion (ω) shown as percent anomalies by dividing by present-day averages. Asterisks denote anomalies statistically significant at the 5% level (Materials and Methods) on the basis of tests of whether changes in the individual terms contribute significantly to the change in (A) ω_D and (B) ω.

Downloaded from https://www.science.org on November 08, 2026

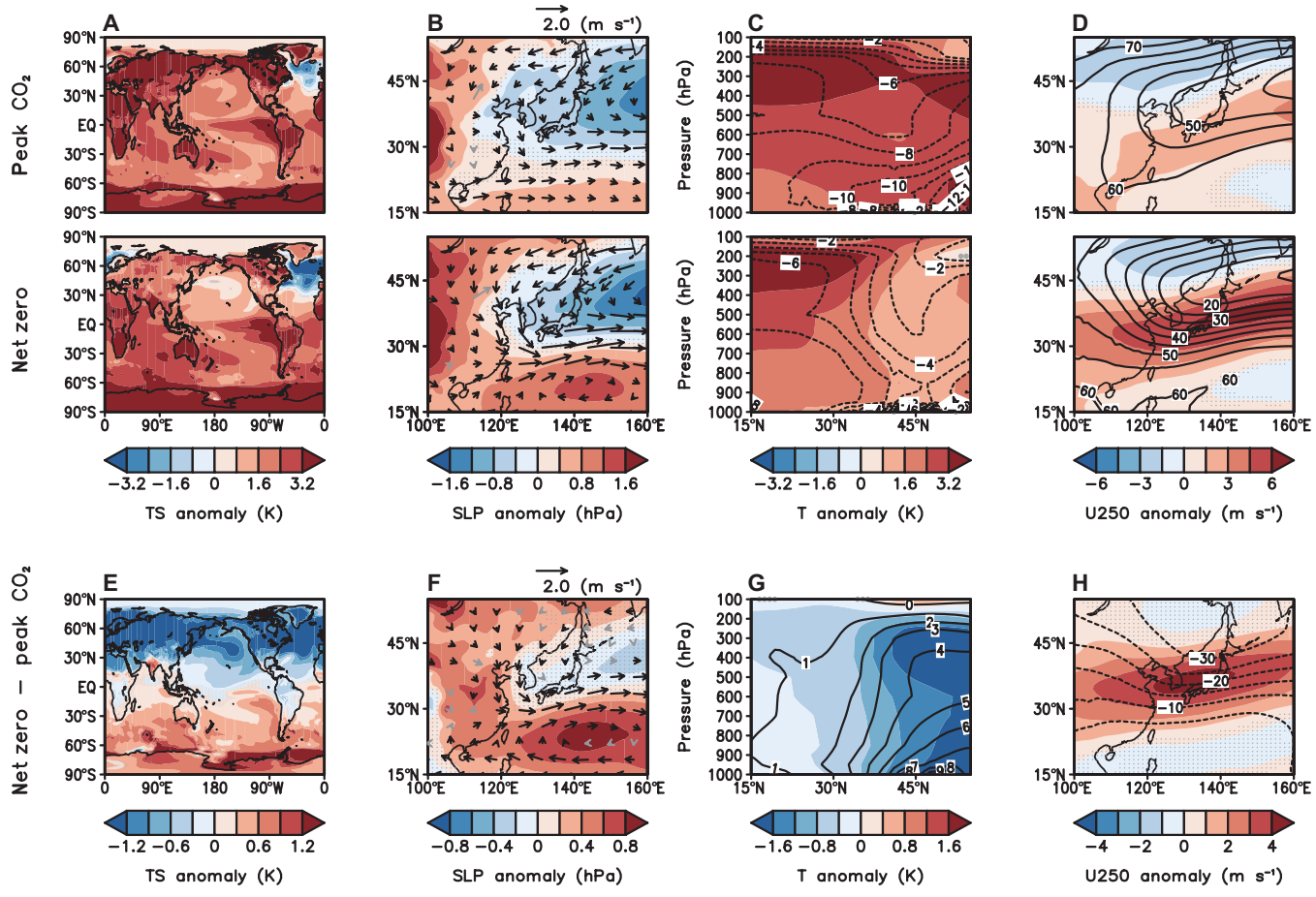


Fig. 6. Changes in climatological planetary-scale environmental conditions. (**A** to **D**) Changes in (A) surface temperature (TS), (B) SLP (shading) and 850-hPa horizontal winds (vectors), (C) East Asian zonal-mean (averaged over 110°E to 150°E) air temperature (T; shading) and air density (contours; unit: 10^{-3} kg m^{-3}), and (D) 250-hPa zonal wind (U250; shading) and 500-hPa geopotential height (contours; unit: m) during JJA for the (upper row) peak CO_2 period and the (lower row) net-zero period, relative to present-day averages. Gray dots indicate regional changes that are not statistically significant at the 5% level (Materials and Methods) for (A) TS, (B) SLP, (C) T, and (D) U250. In (B), wind vectors are shown in black where either zonal or meridional wind component shows significant changes at the 5% level and in gray where changes in both components are not significant. (**E** to **H**) Same as (A) to (D) but showing differences between the net-zero and peak CO_2 periods (net-zero period minus peak CO_2 period).

warming amplifies the high-pressure anomaly over the subtropical western North Pacific (Fig. 6, B and F), together with the influence of the southward ITCZ shift (fig. S10).

Tropical tropospheric temperature adjusts quasi-moist adiabatically to surface temperature changes, resulting in small cooling anomalies during the net-zero period relative to the peak CO_2 period (Fig. 6, C and G). In contrast, warm anomalies are markedly weakened in the NH mid-latitudes (Fig. 6, C and G) because of the combined influence of declining atmospheric CO_2 concentrations and a weakened AMOC. These changes enhance the meridional temperature gradient across the troposphere over East Asia during the net-zero period relative to the peak CO_2 period (Fig. 6, C and G). In addition, the strengthened western North Pacific subtropical high induces anomalous southwesterly winds around 30°N (Fig. 6, B and F), contributing to an enhanced meridional temperature gradient (Fig. 6, C and G). This sharpens the meridional gradient of air density (Fig. 6, C and G), thereby increasing baroclinicity. In turn, the enhanced baroclinicity strengthens the upper-tropospheric westerly jet across the region (Fig. 6, D and H). These changes in the large-scale climatological environment (Fig. 6) modulate the synoptic atmospheric conditions associated with extreme precipitation events (Fig. 4), leading to stronger upward motion through enhanced ω_D (Fig. 5).

DISCUSSION

In this study, we investigate the response of East Asian summer extreme precipitation under a net-zero anthropogenic CO_2 emission scenario. Our results reveal counterintuitive changes in the intensity of extreme precipitation, which continues to increase despite a cooling trend caused by CO_2 reductions, with a corresponding increase in the sensitivity of extreme precipitation intensity to near-surface warming. This suggests that even with aggressive reductions in anthropogenic CO_2 emissions to net zero, the intensity of extreme precipitation may continue to strengthen, potentially leading to enhanced disaster dangers in densely populated regions of East Asian countries.

The intensification in the magnitude and sensitivity (intensification per unit of near-surface warming) of extreme precipitation following net-zero anthropogenic CO_2 emissions is primarily driven by

Downloaded from https://www.science.org on November 08, 2026

an enhanced contribution from dynamic factors (i.e., strengthened upward motion). In contrast, the thermodynamic contribution (i.e., changes in near-surface specific humidity) per unit of near-surface warming is similar between the peak CO_2 and net-zero periods. In the net-zero period relative to the peak CO_2 period, atmospheric conditions associated with extreme precipitation events favor stronger upward motion: an enhanced meridional gradient of temperature (i.e., intensified baroclinicity) and an associated acceleration of the jet together promote stronger ω_D through enhanced $\omega_{D,T}$. Furthermore, the strengthening of the westerly jet contributes to ω_D enhancement through enhanced $\omega_{D,\zeta}$. ω_D is significantly strengthened during the net-zero period, leading to enhanced upward motion and thereby intensifying extreme precipitation events.

Our results show that the enhanced horizontal baroclinicity throughout the troposphere and upper-level jet are the key drivers of the intensification in the magnitude of extreme precipitation following net-zero anthropogenic CO_2 emissions. These originate essentially from changes in the planetary-scale environmental conditions. As atmospheric CO_2 concentration decreases and the AMOC continues to weaken, warming largely declines over the NH extratropics, whereas the SH continues to warm. This hemispheric contrast in temperature change induces a southward shift of the ITCZ. In addition, El Niño–like warming becomes stronger in the tropical Pacific, accompanied by modest additional warming or marginal cooling in the equatorial ocean. These changes enhance the meridional temperature gradient over East Asia. They also contribute to the development of a high-pressure anomaly over the subtropical western North Pacific, accompanied by southwesterly wind anomalies around 30°N. The anomalous southwesterly winds further strengthen the meridional temperature gradient over East Asia, enhancing baroclinicity and subsequently accelerating the upper-tropospheric jet, thereby providing atmospheric conditions favorable for stronger extreme precipitation events.

It is worthwhile to compare the behavior of extreme precipitation under a net-zero anthropogenic CO_2 emission scenario to that of mean precipitation. The JJA mean precipitation exhibits a temporal evolution that is similar to that of extreme precipitation with continued increases and no subsequent decline (fig. S11, A and B), although the magnitude is much smaller. In contrast to extreme precipitation, changes in JJA mean vertical motion account for the mean precipitation changes only over southern East Asia (fig. S11C). Moisture budget analysis indicates that over the central-northern East Asia, the mean precipitation increase is mainly driven by the enhanced transient eddy moisture flux convergence (fig. S11, D to G). The increase in the moisture flux convergence within transient eddies is likely linked to the mechanisms that led to the changes in the extreme precipitation intensity, namely, enhanced baroclinicity, a strengthened upper-level jet, and the resulting intensification of upward motion (Figs. 4 and 5). Therefore, our results suggest that an accurate assessment of the response of the mean precipitation to anthropogenic CO_2 emission changes requires a better understanding of how individual storms within transient eddies respond to the corresponding mean state changes.

The current study possibly carries some uncertainties as we used a single climate model. Nonetheless, self-consistency and physical plausibility of our results show their value in constructing physical climate storylines (*37*). Moreover, the planetary-scale responses to anthropogenic CO_2 reductions, such as the weakening of the hemispheric temperature contrast (SH warming and strong NH extratropical cooling), the weakening (or delayed response) of the AMOC, the southward shift of the ITCZ, and El Niño–like warming, are closely aligned with the previous reports (*6*, *13*, *16*, *34*, *38*), further lending confidence to our results. Albeit differing in experimental design, our parallel analyses using three climate simulations performed under the SSP (Shared Socioeconomic Pathway) 5-3.4-OS scenario (*39*) consistently show continued intensification of extreme precipitation intensity even after atmospheric CO_2 begins to decline from its peak, together with an enhanced meridional temperature gradient and a strengthened westerly jet throughout the troposphere during JJA (fig. S12). Although more detailed analysis of extreme precipitation events such as the diagnosis of ω_D is not feasible because high-frequency three-dimensional datasets are not available, these results from other model simulations support the robustness of our findings.

As the results presented here are influenced by climatic responses operating across a wide range of spatiotemporal scales, the timescale of the continued intensification of extreme precipitation following peak CO_2 concentration is likely affected by multiple factors. These include the peak CO_2 concentration, the trajectory of CO_2 emissions, the model's intrinsic climate sensitivity, and internal climate variability. Systematically quantifying the relative importance of these potential factors, and therefore better constraining the timescale of extreme precipitation responses, requires further development of experimental frameworks. Initiatives such as the flat10MIP (*21*), together with coordinated multimodel and multiensemble experiments considering a broader range of future CO_2 emission scenarios, including variations in cumulative CO_2 emissions, emission rates, the timing of net-zero attainment, and the possible achievement of negative CO_2 emissions (i.e., CO_2 removal), would provide a valuable basis for such investigations.

Our results highlight the importance of a multispatiotemporal scale perspective for understanding extreme weather responses under global warming mitigation. The changes across spatial scales from planetary to synoptic to local and temporal scales from long-term to subdaily play a key role in extreme precipitation responses under a net-zero anthropogenic CO_2 emission scenario. Toward the complete process-level understanding of the extreme precipitation in the current and future climates, there is a pressing need for high-frequency data, such as the variables used in this study, to be stored and made available from Coupled Model Intercomparison Project phase 7 (CMIP7) net-zero and overshoot emission scenarios (*40*). Moreover, using models capable of accurately resolving mesoscale processes [e.g., global storm-resolving models participating in the DYAMOND (DYnamics of the Atmospheric general circulation Modeled On Non-hydrostatic Domains) project (*41*)] would further enhance our understanding of extreme precipitation dynamics under the global warming mitigation strategies.

MATERIALS AND METHODS

Experimental design

We used idealized anthropogenic CO_2 emission reduction simulations conducted using CESM2 (*27*). CESM2 incorporates various components: the atmosphere [Community Atmosphere Model Version 6 (CAM6)], ocean [Parallel Ocean Program Version 2 (POP2) (*42*)], land [Community Land Model Version 5 (CLM5) (*43*)], sea ice [Community Ice CodE Version 5 (CICE5) (*44*)], ice sheet [Community Ice Sheet Model Version 2 (CISM2) (*45*)], river transport [Model for Scale Adaptive River Transport (MOSART) (*46*)], and ocean waves [WaveWatch-III (WW3) (*47*)], all interconnected through a

Downloaded from https://www.science.org on November 08, 2026

coupler. CAM6 has a horizontal resolution of 1.25° in longitude and 0.94° in latitude, with 32 vertical levels and a model top near 2 hPa (~40 km). POP2 has a horizontal resolution of 1.125° in longitude and a latitudinal resolution of ~0.27° near the equator, coarser at higher latitudes, with 60 vertical levels.

Using CESM2, we conducted four ensemble simulations under a net-zero anthropogenic CO_2 emission scenario, each initialized from a different month in 2000 and integrated through December 2400. In these simulations, only anthropogenic CO_2 emissions vary, while all non-CO_2 conditions, such as land use, and non-CO_2 greenhouse gas forcings are held constant at their year-2000 levels, and anthropogenic aerosol emissions are prescribed as the 1995 to 2005 mean. Anthropogenic CO_2 emissions increase linearly to 79.1 $GtCO_2$ per year by 2050, corresponding to the emission level outlined for that year in the SSP 5-8.5 scenario (*39*), and then decline linearly to reach net zero in 2123. Thereafter, net-zero anthropogenic CO_2 emissions are maintained through 2400. For this scenario, our analysis focuses on two 31-year periods: (i) 2091 to 2121, centered on the year of peak atmospheric CO_2 concentration, corresponding to the maximum in the 31-year moving average ("peak CO_2" period), and (ii) 2170 to 2200, the final 31 years of the 22nd century under sustained net-zero CO_2 emissions ("net-zero" period).

In addition, a 200-year present-day (control) simulation was conducted, initialized with anthropogenic CO_2 emission levels from the year 2000 and run without any additional emissions. In this simulation, atmospheric CO_2 concentrations gradually decline because of natural CO_2 uptake. To minimize the impacts of this decline, only the first 50 years are used to represent present-day climate conditions.

Extreme precipitation

Extreme precipitation events are defined as 6-hour precipitation exceeding the 99th percentile at each grid point during June to August within each analysis period (e.g., 18,400 and 11,408 values were used to estimate the 99th percentile for the 50-year present-day simulation and the 31-year peak CO_2 and net-zero periods, respectively). The mean 6-hour precipitation of these events is used to represent extreme precipitation intensity in each period.

Decomposing vertical motion

Vertical motion at 500 hPa (ω) is decomposed as $\omega = \omega_D + \alpha\omega_D$, which can also be written as $\omega = \omega_D(1+\alpha)$, where ω_D represents the component driven by adiabatic quasi-geostrophic forcing, and α represents the amplification factor primarily associated with diabatic heating feedback. ω_D is estimated using the conventional form of the quasi-geostrophic omega equation (*48*, *49*) which decomposes into contributions from temperature-advection ($\omega_{D,T}$) and vorticity-advection ($\omega_{D,\zeta}$) terms, expressed as

$$\left\{f^2\frac{\partial^2(\cdot)}{\partial p^2} + \nabla_p\cdot\left[S\nabla_p(\cdot)\right]\right\}\omega = \frac{R_d\pi}{p}\nabla_p{}^2\left(\mathbf{V}_g\cdot\nabla_p\theta\right) + f\frac{\partial}{\partial p}\left(\mathbf{V}_g\cdot\nabla_p\zeta_g\right)$$

where f is the Coriolis parameter, p is the pressure, ∇_p is the gradient operator on a pressure surface, S is the static stability ($-\frac{R_d\pi}{p}\frac{\partial\theta}{\partial p}$, where R_d is the gas constant for dry air, π is the Exner function, and θ is the potential temperature), ω is the pressure velocity, $\mathbf{V}_g$ is the geostrophic wind and ζ_g is the geostrophic relative vorticity. The inverted first and second terms on the right-hand side correspond to $\omega_{D,T}$ and $\omega_{D,\zeta}$, respectively. We directly computed $\omega_{D,T}$ and $\omega_{D,\zeta}$, summed them to obtain ω_D (i.e., $\omega_D = \omega_{D,T} + \omega_{D,\zeta}$) using CESM2 simulation outputs, and estimated $\alpha\omega_D$ as the difference between ω and ω_D.

Statistical significance test

Using the first 100 years of the CESM2 present-day simulation, we repeated the presented analyses 1000 times, each time randomly selecting the same number of samples as in the "peak CO_2" or "net-zero" period (i.e., 31 years). Although the use of 100 years of data may incorporate the effects of natural CO_2 uptake from the atmosphere and therefore overestimate internal climate variability, this approach was adopted to ensure a sufficiently large sample size for estimating the percentile ranges. To better estimate ranges of internal variability, the 100-year present-day data are converted to anomalies by removing their mean state before resampling. For analyses of extreme precipitation–related fields, extreme events were first identified using thresholds estimated from the first 50 years to preserve the present-day extreme precipitation characteristics as closely as possible. The same anomaly-based resampling procedure was then applied only to the time steps associated with those selected events. Results within the 2.5th to 97.5th percentile range of these 1000 samples were deemed statistically insignificant at the 5% level. We adopted this strategy because some analyses in this study use potentially nonindependent values, such as averages of instantaneous fields at the start and end of each 6-hour period. Significance tests for extreme precipitation–related fields are conducted using the original datasets, whereas seasonal-mean fields are tested using detrended data to minimize the influence of declining atmospheric CO_2 concentrations on the estimated 2.5th to 97.5th percentile ranges.

Decomposing extreme precipitation responses

Extreme precipitation responses are separated into contributions from thermodynamic and dynamic factors, as well as a nonlinear component, using a conventional decomposition approach. Owing to limitations in the availability of 6-hourly three-dimensional datasets, we estimate the physical scaling diagnostic for extreme precipitation events (*5*) using the approximate method (*50*, *51*), expressed as

$$\text{Dynamic contribution} = q_{\text{present-day}} \times \Delta\omega$$

$$\text{Thermodynamic contribution} = \omega_{\text{present-day}} \times \Delta q$$

$$\text{Nonlinear component} = \Delta\omega \times \Delta q$$

where q is the near-surface specific humidity, and ω is the vertical velocity at 500 hPa, both corresponding to 6-hour extreme precipitation events at each grid point. The subscript "present-day" refers to the present-day value, and Δ indicates changes relative to present-day averages.

Supplementary Materials

This PDF file includes:

Figs. S1 to S12

REFERENCES

1. M. R. Allen, W. J. Ingram, Constraints on future changes in climate and the hydrologic cycle. *Nature* **419**, 224–232 (2002).
2. S.-K. Min, X. Zhang, F. W. Zwiers, G. C. Hegerl, Human contribution to more-intense precipitation extremes. *Nature* **470**, 378–381 (2011).

Downloaded from https://www.science.org on November 08, 2026

3. X. Zhang, H. Wan, F. W. Zwiers, G. C. Hegerl, S.-K. Min, Attributing intensification of precipitation extremes to human influence. *Geophys. Res. Lett.* **40**, 5252–5257 (2013).
4. S. Paik, S.-K. Min, X. Zhang, M. G. Donat, A. D. King, Q. Sun, Determining the anthropogenic greenhouse gas contribution to the observed intensification of extreme precipitation. *Geophys. Res. Lett.* **47**, e2019GL086875 (2020).
5. S. Pfahl, P. A. O'Gorman, E. M. Fischer, Understanding the regional pattern of projected future changes in extreme precipitation. *Nat. Clim. Change* **7**, 423–427 (2017).
6. J.-Y. Lee, J. Marotzke, G. Bala, L. Cao, S. Corti, J. P. Dunne, F. Engelbrecht, E. Fischer, J. C. Fyfe, C. Jones, A. Maycock, J. Mutemi, O. Ndiaye, S. Panickal, T. Zhou, "Future global climate: Scenario-based projections and near-term information" in *Climate Change 2021: The Physical Science Basis. Contribution of Working Group I to the Sixth Assessment Report of the Intergovernmental Panel on Climate Change*, V. Masson-Delmotte, P. Zhai, A. Pirani, S. L. Connors, C. Péan, S. Berger, N. Caud, Y. Chen, L. Goldfarb, M. I. Gomis, M. Huang, K. Leitzell, E. Lonnoy, J. B. R. Matthews, T. K. Maycock, T. Waterfield, O. Yelekçi, R. Yu, B. Zhou, Eds. (Cambridge Univ. Press, 2021), pp. 553–672.
7. S. Paik, S.-I. An, S.-K. Min, A. D. King, S.-K. Kim, Emergent constraints on future extreme precipitation intensification: From global to continental scales. *Weather Clim. Extrem.* **42**, 100613 (2023).
8. P. A. O'Gorman, Precipitation extremes under climate change. *Curr. Clim. Change Rep.* **1**, 49–59 (2015).
9. J. Nie, A. H. Sobel, D. A. Shaevitz, S. Wang, Dynamic amplification of extreme precipitation sensitivity. *Proc. Nat. Acad. Sci. U.S.A.* **115**, 9467–9472 (2018).
10. United Nations Framework Convention on Climate Change (UNFCCC), Adoption of the Paris Agreement, 21st Conference of the Parties (2015); http://unfccc.int/resource/docs/2015/cop21/eng/l09r01.pdf.
11. C. D. Jones, T. L. Frölicher, C. Koven, A. H. MacDougall, H. D. Matthews, K. Zickfeld, J. Rogelj, K. B. Tokarska, N. P. Gillett, T. Ilyina, M. Meinshausen, N. Mengis, R. Séférian, M. Eby, F. A. Burger, The Zero Emissions Commitment Model Intercomparison Project (ZECMIP) contribution to C4MIP: Quantifying committed climate changes following zero carbon emissions. *Geosci. Model Dev.* **12**, 4375–4385 (2019).
12. A. H. MacDougall, J. Mallett, D. Hohn, N. Mengis, Substantial regional climate change expected following cessation of CO_2 emissions. *Environ. Res. Lett.* **17**, 114046 (2022).
13. J. Schwinger, A. Asaadi, N. Goris, H. Lee, Possibility for strong northern hemisphere high-latitude cooling under negative emissions. *Nat. Commun.* **13**, 1095 (2022).
14. L. J. Cassidy, A. D. King, J. R. Brown, A. H. MacDougall, T. Ziehn, S.-K. Min, C. D. Jones, Regional temperature extremes and vulnerability under net zero CO_2 emissions. *Environ. Res. Lett.* **19**, 014051 (2024).
15. L. J. Cassidy, A. D. King, J. R. Brown, T. Ziehn, A. Borowiak, Evolution of heat extremes under net-zero CO_2 emissions. *Earth's Future* **13**, e2024EF005399 (2025).
16. A. D. King, T. Ziehn, M. Chamberlain, A. R. Borowiak, J. R. Brown, L. Cassidy, A. J. Dittus, M. Grose, N. Maher, S. Paik, S. E. Perkins-Kirkpatrick, A. Sengupta, Exploring climate stabilisation at different global warming levels in ACCESS-ESM-1.5. *Earth Syst. Dynam.* **15**, 1353–1383 (2024).
17. C. Liu, S.-I. An, J. Zhao, S.-W. Son, F.-F. Jin, R. Zhan, Hemispheric asymmetric response of tropical cyclones to CO_2 emission reduction. *npj Clim. Atmos. Sci.* **7**, 83 (2024).
18. A. Borowiak, A. D. King, J. R. Brown, C. D. Jones, M. Grose, Climate stabilisation under net zero CO_2 emissions. *Earth's Future* **13**, e2024EF005678 (2025).
19. M. Moon, S.-K. Min, J.-E. Chu, S.-I. An, S.-W. Son, H. Ramsay, Z. Wang, Tropical cyclone response to ambitious decarbonization scenarios. *npj Clim. Atmos. Sci.* **8**, 228 (2025).
20. S.-W. Park, J.-H. Mun, H. Lee, N. J. Steinert, S.-I. An, J. Shin, J.-S. Kug, Continued permafrost ecosystem carbon loss under net-zero and negative emissions. *Sci. Adv.* **11**, eadn8819 (2025).
21. B. M. Sanderson, V. Brovkin, R. A. Fisher, D. Hohn, T. Ilyina, C. D. Jones, T. Koenigk, C. Koven, H. Li, D. M. Lawrence, P. Lawrence, S. Liddicoat, A. H. MacDougall, N. Mengis, Z. Nicholls, E. O'Rourke, A. Romanou, M. Sandstad, J. Schwinger, R. Séférian, L. T. Sentman, I. R. Simpson, C. Smith, N. J. Steinert, A. L. S. Swann, J. Tjiputra, T. Ziehn, flat10MIP: An emissions-driven experiment to diagnose the climate response to positive, zero and negative CO_2 emissions. *Geosci. Model Dev.* **18**, 5699–5724 (2025).
22. J. Shin, J.-S. Kug, S.-W. Park, J. Kam, S.-I. An, S.-E. Park, H. Oh, S.-W. Yeh, S. Jeong, C.-K. Park, J.-S. Kim, Negative CO_2 emissions for long-term mitigation of extremes in land hydrological cycle. *Nat. Commun.* **17**, 4347 (2026).
23. S. Moon, N. Utsumi, J.-H. Jeong, J.-H. Yoon, S.-Y. S. Wang, H. Shiogama, H. Kim, Anthropogenic warming induced intensification of summer monsoon frontal precipitation over East Asia. *Sci. Adv.* **9**, eadh4195 (2023).
24. S. He, T. Takemi, Future changes of extreme precipitation and related atmospheric conditions in East Asia under global warming projected in large ensemble climate prediction data. *J. Clim.* **37**, 5171–5186 (2024).
25. S.-Y. Jo, M.-G. Seong, S.-K. Min, J.-S. Kug, S.-W. Yeh, S.-I. An, S.-W. Son, J. Shin, Hysteresis behaviors in East Asian extreme precipitation frequency to CO_2 pathway. *Geophys. Res. Lett.* **49**, e2022GL099814 (2022).
26. M. B. Miah, J.-Y. Park, M.-U. Lee, W. Jeon, Y.-H. Byun, H. M. Sung, J. G. Hong, M. J. Uddin, S. K. Mondal, Irreversibility of extreme precipitation intensity in global monsoon areas under multiple carbon neutrality scenarios. *Weather Clim. Extrem.* **51**, 100843 (2026).
27. G. Danabasoglu, J.-F. Lamarque, J. Bacmeister, D. A. Bailey, A. K. DuVivier, J. Edwards, L. K. Emmons, J. Fasullo, R. Garcia, A. Gettelman, C. Hannay, M. M. Holland, W. G. Large, P. H. Lauritzen, D. M. Lawrence, J. T. M. Lenaerts, K. Lindsay, W. H. Lipscomb, M. J. Mills, R. Neale, K. W. Oleson, B. Otto-Bliesner, A. S. Phillips, W. Sacks, S. Tilmes, L. van Kampenhout, M. Vertenstein, A. Bertini, J. Dennis, C. Deser, C. Fischer, B. Fox-Kemper, J. E. Kay, D. Kinnison, P. J. Kushner, V. E. Larson, M. C. Long, S. Mickelson, J. K. Moore, E. Nienhouse, L. Polvani, P. J. Rasch, W. G. Strand, The Community Earth System Model version 2 (CESM2). *J. Adv. Model. Earth Syst.* **12**, e2019MS001916 (2020).
28. A. F. Prein, P. A. Mooney, J. M. Done, The multi-scale interactions of atmospheric phenomenon in mean and extreme precipitation. *Earth's Future* **11**, e2023EF003534 (2023).
29. K. Konstali, C. Spensberger, T. Spengler, A. Sorteberg, Global attribution of precipitation to weather features. *J. Clim.* **37**, 1181–1196 (2024).
30. W.-M. Tsai, S. Duan, T. A. O'Brien, J. L. Catto, P. A. Ullrich, Y. Zhou, L. R. Leung, Z. Feng, W. R. Boos, D. L. Suhas, F. Ahmed, J. D. Neelin, Co-occurring atmospheric features and their contributions to precipitation extremes. *J. Geophys. Res. Atmos.* **130**, e2024JD041687 (2025).
31. G. J. Huffman, D. T. Bolvin, R. Joyce, E. J. Nelkin, J. Tan, D. Braithwaite, K. Hsu, O. A. Kelley, P. Nguyen, S. Sorooshian, D. C. Watters, B. J. West, P. Xie, "NASA Global Precipitation Measurement (GPM) Integrated Multi-satellitE Retrievals for GPM (IMERG) Version 07" (Algorithm Theoretical Basis Document (ATBD), National Aeronautics and Space Administration, 2023).
32. H. Hersbach, B. Bell, P. Berrisford, S. Hirahara, A. Horányi, J. Muñoz-Sabater, J. Nicolas, C. Peubey, R. Radu, D. Schepers, A. Simmons, C. Soci, S. Abdalla, X. Abellan, G. Balsamo, P. Bechtold, G. Biavati, J. Bidlot, M. Bonavita, G. De Chiara, P. Dahlgren, D. Dee, M. Diamantakis, R. Dragani, J. Flemming, R. Forbes, M. Fuentes, A. Geer, L. Haimberger, S. Healy, R. J. Hogan, E. Hólm, M. Janisková, S. Keeley, P. Laloyaux, P. Lopez, C. Lupu, G. Radnoti, P. de Rosnay, I. Rozum, F. Vamborg, S. Villaume, J.-N. Thépaut, The ERA5 global reanalysis. *Q. J. R. Meteorol. Soc.* **146**, 1999–2049 (2020).
33. L. C. Jackson, R. Kahana, T. Graham, M. A. Ringer, T. Woollings, J. V. Mecking, R. A. Wood, Global and European climate impacts of a slowdown of the AMOC in a high resolution GCM. *Clim. Dyn.* **45**, 3299–3316 (2015).
34. J.-S. Kug, J.-H. Oh, S.-I. An, S.-W. Yeh, S.-K. Min, S.-W. Son, J. Kam, Y.-G. Ham, J. Shin, Hysteresis of the intertropical convergence zone to CO_2 forcing. *Nat. Clim. Change* **12**, 47–53 (2022).
35. B. Wang, R. Wu, X. Fu, Pacific–East Asian teleconnection: How does ENSO affect East Asian climate? *J. Clim.* **13**, 1517–1536 (2000).
36. J.-H. Oh, J.-S. Kug, S.-I. An, F.-F. Jin, M. J. McPhaden, J. Shin, Emergent climate change patterns originating from deep ocean warming in climate mitigation scenarios. *Nat. Clim. Change* **14**, 260–266 (2024).
37. M. Baldissera Pacchetti, L. Coulter, S. Dessai, T. G. Shepherd, J. Sillmann, B. Van Den Hurk, Varieties of approaches to constructing physical climate storylines: A review. *Wiley Interdiscip. Rev. Clim. Change* **15**, e869 (2024).
38. S.-I. An, J. Shin, S.-W. Yeh, S.-W. Son, J.-S. Kug, S.-K. Min, H.-J. Kim, Global cooling hiatus driven by an AMOC overshoot in a carbon dioxide removal Scenario. *Earth's Future* **9**, e2021EF002165 (2021).
39. B. C. O'Neill, C. Tebaldi, D. P. van Vuuren, V. Eyring, P. Friedlingstein, G. Hurtt, R. Knutti, E. Kriegler, J.-F. Lamarque, J. Lowe, G. A. Meehl, R. Moss, K. Riahi, B. M. Sanderson, The Scenario Model Intercomparison Project (ScenarioMIP) for CMIP6. *Geosci. Model Dev.* **9**, 3461–3482 (2016).
40. D. P. Van Vuuren, B. C. O'Neill, C. Tebaldi, B. M. Sanderson, L. P. Chini, P. Friedlingstein, T. Hasegawa, K. Riahi, B. Govindasamy, N. Bauer, V. Eyring, C. M. N. Fall, K. Frieler, M. J. Gidden, L. K. Gohar, A. Högner, A. D. Jones, J. Kikstra, A. King, R. Knutti, E. Kriegler, P. Lawrence, C. Lennard, J. Lowe, C. Mathison, S. Mehmood, Z. Nicholls, L. F. Prado, Q. Zhang, S. K. Rose, A. C. Ruane, M. Sandstad, C.-F. Schleussner, R. Seferian, J. Sillmann, C. Smith, A. A. Sörensson, S. Panickal, K. Tachiiri, N. Vaughan, S. S. Vishwanathan, T. Yokohata, M. Zecchetto, T. Ziehn, The Scenario Model Intercomparison Project for CMIP7 (ScenarioMIP-CMIP7). *Geosci. Model Dev.* **19**, 2627–2656 (2026).
41. B. Stevens, M. Satoh, L. Auger, J. Biercamp, C. S. Bretherton, X. Chen, P. Düben, F. Judt, M. Khairoutdinov, D. Klocke, C. Kodama, L. Kornblueh, S.-J. Lin, P. Neumann, W. M. Putman, N. Röber, R. Shibuya, B. Vanniere, P. L. Vidale, N. Wedi, L. Zhou, DYAMOND: The DYnamics of the Atmospheric general circulation Modeled On Non-hydrostatic Domains. *Prog. Earth Planet. Sci.* **6**, 61 (2019).
42. R. Smith, P. Jones, B. Briegleb, F. Bryan, G. Danabasoglu, J. Dennis, J. Dukowicz, C. Eden, B. Fox-Kemper, P. Gent, M. Hecht, S. Jayne, M. Jochum, W. Large, K. Lindsay, M. Maltrud, N. Norton, S. Peacock, M. Vertenstein, S. Yeager, "The Parallel Ocean Program (POP) reference manual: Ocean component of the Community Climate System Model (CCSM) and Community Earth System Model (CESM)" (LAUR-10-01853, Los Alamos National Laboratory, 2010).
43. D. M. Lawrence, R. A. Fisher, C. D. Koven, K. W. Oleson, S. C. Swenson, G. Bonan, N. Collier, B. Ghimire, L. van Kampenhout, D. Kennedy, E. Kluzek, P. J. Lawrence, F. Li, H. Li, D. Lombardozzi, W. J. Riley, W. J. Sacks, M. Shi, M. Vertenstein, W. R. Wieder, C. Xu, A. A. Ali, A. M. Badger, G. Bisht, M. van den Broeke, M. A. Brunke, S. P. Burns, J. Buzan, M. Clark,

Downloaded from https://www.science.org on November 08, 2026

A. Craig, K. Dahlin, B. Drewniak, J. B. Fisher, M. Flanner, A. M. Fox, P. Gentine, F. Hoffman, G. Keppel-Aleks, R. Knox, S. Kumar, J. Lenaerts, L. R. Leung, W. H. Lipscomb, Y. Lu, A. Pandey, J. D. Pelletier, J. Perket, J. T. Randerson, D. M. Ricciuto, B. M. Sanderson, A. Slater, Z. M. Subin, J. Tang, R. Q. Thomas, M. Val Martin, X. Zeng, The Community Land Model version 5: description of new features, benchmarking, and impact of forcing uncertainty. *J. Adv. Model. Earth Syst.* **11**, 4245–4287 (2019).
44. E. C. Hunke, W. H. Lipscomb, A. K. Turner, N. Jeffery, S. Elliott, "CICE: the Los Alamos Sea Ice Model Documentation and Software User's Manual Version 5.1." (Tech. Rep. LA-CC-06-012, Los Alamos National Laboratory, 2015).
45. W. H. Lipscomb, S. F. Price, M. J. Hoffman, G. R. Leguy, A. R. Bennett, S. L. Bradley, K. J. Evans, J. G. Fyke, J. H. Kennedy, M. Perego, D. M. Ranken, W. J. Sacks, A. G. Salinger, L. J. Vargo, P. H. Worley, Description and evaluation of the Community Ice Sheet Model (CISM) v2.1. *Geosci. Model Dev.* **12**, 387–424 (2019).
46. H. Li, M. S. Wigmosta, H. Wu, M. Huang, Y. Ke, A. M. Coleman, L. R. Leung, A physically based runoff routing model for land surface and earth system models. *J. Hydrometeorol.* **14**, 808–828 (2013).
47. H. L. Tolman, "User manual and system documentation of WAVEWATCH III™ version 3.14" (Technical Note, NOAA/NWS/NCEP/MMAB, 2009).
48. B. J. Hoskins, I. Draghici, H. C. Davies, A new look at the ω-equation. *Q. J. R. Meteorol. Soc.* **104**, 31–38 (1978).
49. J. R. Holton, G. J. Hakim, "Quasi-geostrophic analysis" in *An Introduction to Dynamic Meteorology* (Academic Press, ed. 5, 2013), pp. 171–211.
50. P. Huang, S.-P. Xie, K. Hu, G. Huang, R. Huang, Patterns of the seasonal response of tropical rainfall to global warming. *Nat. Geosci.* **6**, 357–361 (2013).
51. S.-M. Long, S.-P. Xie, W. Liu, Uncertainty in tropical rainfall projections: atmospheric circulation effect and the ocean coupling. *J. Clim.* **29**, 2671–2687 (2016).

Acknowledgments
Funding: This study was supported by the National Research Foundation of Korea (NRF) grant funded by the Korean government (MSIT) (RS-2025-02310080) and by the Korea Meteorological Administration Research and Development Program (grant: RS-2025-02313090). S.P. was supported by the National Research Foundation of Korea (NRF) grant funded by the Korean government (MSIT) (RS-2026-25475832). D.K. was supported by the Korea Meteorological Administration Research and Development Program under Grant (RS-2025-02221669). S.-I.A. was supported by the Yonsei Fellowship, funded by L. Y. Jae. A.D.K. was supported by an ARC Future Fellowship (FT240100306). Model simulation and data transfer were supported by the National Supercomputing Center with supercomputing resources including technical support (KSC-2021-CHA-0030), the National Center for Meteorological Supercomputer of the Korea Meteorological Administration (KMA), and the Korea Research Environment Open NETwork (KREONET), respectively. **Author contributions:** Conceptualization: S.P., D.K., and S.-I.A. Methodology: S.P. and D.K. Software: S.P. Validation: S.P. Formal analysis: S.P. Investigation: S.P. Resources: S.P. and S.-E.P. Data curation: S.P. Visualization: S.P. Writing—original draft: S.P. Writing—review and editing: S.P., D.K., S.-I.A., S.-E.P., A.D.K., S.-K.M., C.L., and J.S. Supervision: D.K. and S.-I.A. Project administration: S.P., D.K., and S.-I.A. Funding acquisition: S.P., D.K., and S.-I.A. **Competing interests:** The authors declare that they have no competing interests. **Data, code, and materials availability:** CESM2 simulation datasets used in this study are available at https://doi.org/10.5281/zenodo.19941365 and from S.P. upon request. IMERG observations were obtained from https://arthurhouhttps.pps.eosdis.nasa.gov/gpmdata/ (the IMERG GPM data are freely available to the public after an email registration, as required by NASA's data policy). ERA5 reanalysis datasets were obtained from https://doi.org/10.24381/cds.adbb2d47 and https://doi.org/10.24381/cds.bd0915c6. Quasi-geostrophic omega is calculated on the basis of https://github.com/miniufo/xinvert/blob/master/docs/source/notebooks/11_Omega_equation.ipynb. The analyses were performed using NCAR Command Language (version 6.6.2), Climate Data Operators (version 2.5.0), and Python (version 3.11.15). All figures were generated with the Grid Analysis and Display System (version 2.1.0.oga.1). All data and code needed to evaluate and reproduce the results in the paper are present in the paper and/or the Supplementary Materials.

Submitted 8 October 2025
Accepted 8 September 2026
Published 9 October 2026
10.1126/sciadv.aec9366

Downloaded from https://www.science.org on November 08, 2026

ScienceAdvances

Intensification of East Asian summer extreme precipitation under a net-zero anthropogenic CO_2 emission scenario

Seungmok Paik, Daehyun Kim, Soon-Il An, So-Eun Park, Andrew D. King, Seung-Ki Min, Chao Liu, and Jongsoo Shin

Sci. Adv. **12** (41), eaec9366. DOI: 10.1126/sciadv.aec9366

View the article online
https://www.science.org/doi/10.1126/sciadv.aec9366
Permissions
https://www.science.org/help/reprints-and-permissions

Downloaded from https://www.science.org on November 08, 2026

Use of this article is subject to the Terms of service

Science Advances (ISSN 2375-2548) is published by the American Association for the Advancement of Science. 1200 New York Avenue NW, Washington, DC 20005. The title *Science Advances* is a registered trademark of AAAS.

Copyright © 2026 The Authors, some rights reserved; exclusive licensee American Association for the Advancement of Science. No claim to original U.S. Government Works. Distributed under a Creative Commons Attribution NonCommercial License 4.0 (CC BY-NC).